Adsorption of Azo Dyes by a Novel Bio-Nanocomposite Based on Whey Protein Nanofibrils and Montmorillonite: Equilibrium Isotherm and Kinetic Modeling

Shabboo RahimiAqdam[a], Daniel E. Otzen[b] and Dina Morshedi[a*]

[a] Bioprocess Engineering Research Group, Industrial and Environmental Biotechnology, National Institute of Genetic Engineering and Biotechnology, Tehran, Iran.

[b] Interdisciplinary Nanoscience Centre (iNANO), Department of Molecular Biology and Genetics, Aarhus University, 8000 Aarhus C, Denmark

*Corresponding author: D. Morshedi, Tel: +98 2144787423
E-mail: morshedi@nigeb.ac.ir, morshedidina@yahoo.com

Abstract: Excessive discharge of hazardous azo dyes into water is a worldwide concern. Here, we develop an approach to remediate dye solutions by fabricating a strong bio-nanocomposite, based on whey protein concentrate nanofibrils (WPF) and montmorillonite nano-clay (MMT). Nanofibrils lead to a uniform dispersion of MMT in the whey protein matrix and also reinforce the nanocomposite. The adsorption efficacy was monitored in a batch system, using cationic dyes (Chrysoidine-G, Bismarck brown-R), reactive dyes (reactive black-5, reactive orange-16), acid dyes (acid red-88, acid red-114), and direct dyes (direct violet-51, Congo red). WPF/MMT adsorbed all the studied dyes; cationic dyes quicker (>82%, after 4 h) and reactive dyes slower. Then, the effect of dye concentration, contact time and adsorbent dose on Chrysoidine-G adsorption was explored. WPF/MMT showed a high removal (>93%) for a wide concentration range of Chrysoidine-G. Equilibrium adsorption parameters were reasonably fitted with a linear (Nernst) isotherm model, while kinetic data were fitted with pseudo-second-order and intra-particle diffusion models. To characterize the nanocomposite, we used SEM, FT-IR, XRD and BET techniques. The results of BET, isotherm and kinetic analysis all indicated the existence of an unlimited number of absorption sites, *i.e.* no saturation was achieved under our experimental conditions. We conclude that WPF/MMT is a green adsorbent with potential use for wastewater treatment and related purposes.

Keywords: Protein-based nanocomposite; Whey Protein Concentrate (WPC); Nano-clay; Chrysoidine-G; Wastewater remediation

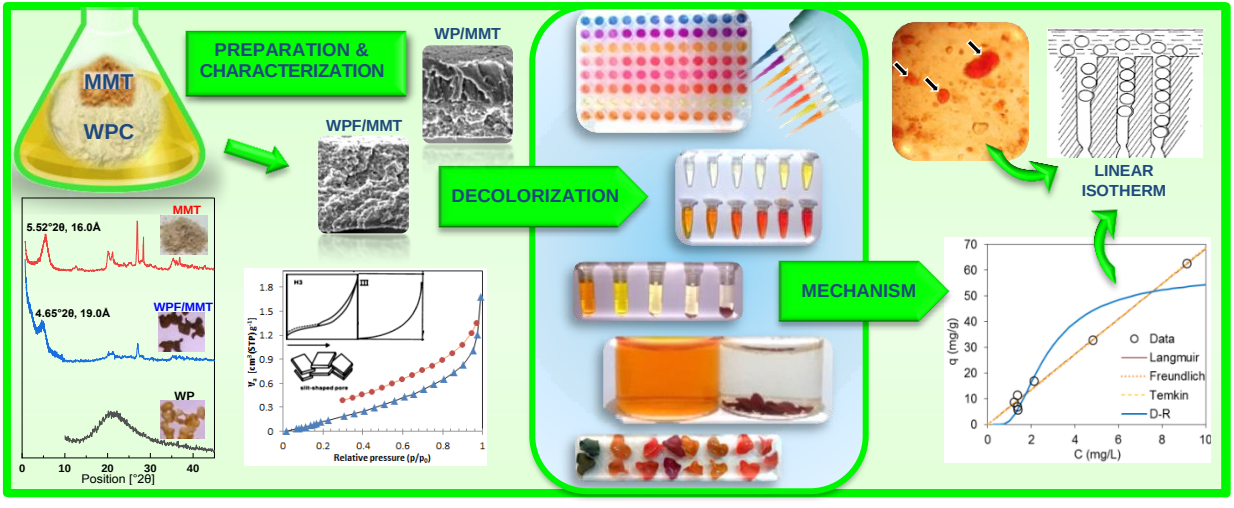
MMT
WPC
PREPARATION & CHARACTERIZATION
WP/MMT
WPF/MMT
DECOLORIZATION
MECHANISM
LINEAR ISOTHERM
MMT
5.52°2θ, 16.0Å
WPF/MMT
4.65°2θ, 19.0Å
WP
Position [°2θ]
H3
H1
slit-shaped pore
Relative pressure (p/p0)
Data
Langmuir
Freundlich
Temkin
D-R
q (mg/g)
C (mg/L)

Highlights:

- We produced a novel bio-nanocomposite using whey nanofibrils and nano-clay
- Nanofibrils help disperse MMT particles uniformly in the WP matrix
- This composite adsorbs cationic, anionic, direct and reactive azo dyes with different kinetics
- Adsorption isotherms and kinetics are studied in detail
- WPF/MMT has Infinitive (unsaturatable) adsorption sites

1. Introduction

The release of large amounts of unprocessed wastewater into the environment is a global problem with significant health and environmental impacts. For instance, 10-15% of dyes used in dyeing processes are discharged in this way (Ghosh, Hazra, Naik, & Ghosh, 2015). Azo dyes, because of their cheap and straightforward synthesis, account for 60-70% of total dye production in the world (Fernández, Larrechi, & Callao, 2010; Ghosh et al., 2015). However, due to their complex structures and aromatic content, they are not naturally degraded (Forgacs, Cserhati, & Oros, 2004), making them major sources of aqueous pollutants worldwide. Besides changing the appearance and color of water, they inhibit photosynthesis through the absorption of sunlight and also lead to carcinogenic and mutagenic metabolites (Fernández et al., 2010; Leung, Lo, & Chan, 2015).

Wastewater treatment generally includes biological, chemical, and physical methods. Common remediation techniques for dyes include electrochemical destruction, filtration, sedimentation, coagulation and flocculation, ion exchange, adsorption, exposure to light and microbiological treatment (Lucas, Algarra, Jiménez-Jiménez, Rodríguez-Castellón, & Peres, 2013; Nawaz & Ahsan, 2014; Şengil & Özacar, 2009; Vandevivere, Bianchi, & Verstraete, 1998; Weng, Lin, & Yuan, 2013). Adsorption techniques are most widespread because of their low cost, high efficiency, simplicity, and usual absence of by-products. Nevertheless, remediation methods have some limitations and sometimes produce more dangerous by-products. Additionally, due to the vast diversity of the chemo-physical and structural properties of azo dyes, there are no stand-alone methods to decolorize wastewater completely (Han et al., 2019; Katheresan, Kansedo, & Lau, 2018). However, the growth of industries with dye by-product pollution coupled with shrinking water resources makes it imperative to develop new methods and materials to recycle wastewater.

In this regard, natural materials, bio-polymers, and bio-nanocomposites have received much attention as potential adsorbents. Natural materials are environmentally friendly as they are biodegradable and biocompatible. Thanks to their structural and chemical diversity, protein-based adsorbents have distinct advantages over conventional polysaccharide-based adsorbents such as cellulose, chitosan and lignin (Markandeya, Dhiman, Shukla, & Kisku, 2017; Pandey, Shukla, & Singh, 2017). Additionally, some proteins can self-assemble and convert into highly ordered nanofibrils which resist elevated temperature and salt concentrations and also show strength and stiffness comparable to that of steel and silk (Cherny & Gazit, 2008; Jung, Gasiorowski, & Collier, 2010).

Whey protein is a well-known source of protein that easily self-assembles into nanofibrils. Whey is a byproduct of cheese manufacturing, with roughly 50 million tons of unused whey per year (Azevedo et al., 2015). Thanks to whey's high carbohydrate and protein content, its release as waste into the environment has a significant negative impact due to eutrophication (Palmieri, Forleo, & Salimei, 2017; Prazeres, Carvalho, & Rivas, 2012; Wakai & Almenar, 2015). Thus, exploitation of whey can both mobilize unwanted waste material and generate novel functionalities. It is particularly useful that whey can form gels, hydrogels, and also proteinaceous nanofibrils (Farjami, Madadlou, & Labbafi, 2015). Such nanofibrils can reinforce composite mixtures by increasing gel viscosity and strength (Akkermans, Van der Goot, Venema, Van der Linden, & Boom, 2008) On top of this,

proteinaceous nanofibrils show excellent ability to absorb azo dyes and other toxic pollutants such as arsenic from aqueous solutions (Bolisetty, Reinhold, Zeder, Orozco, & Mezzenga, 2017; Morshedi, Mohammadi, Boojar, & Aliakbari, 2013). Another dual-purpose (*i.e.* promoting both structural strength and absorption) dye adsorbent is montmorillonite nano-clay (MMT) (Mukhopadhyay et al., 2020), whose basic structure is a central alumina octahedral sheet sandwiched between two tetrahedral silica sheets. These ~1 nm aluminosilicate layers can be extended indefinitely in the x-y plane. The layers are stabilized by electrostatic and Van der Waals forces with a fixed interlayer distance, which varies depending on the cation. The cations can be exchanged with organic cations (such as dye molecules), leading to increased interlayer distance (d-spacing). Since the layers are overall negatively charged, they reversibly bind cationic dyes (Adeyemo, Adeoye, & Bello, 2017; Kausar et al., 2018; Mittal, 2009).

To exploit and combine the advantages of WPF and MMT, we have produced a new bio-nanocomposite (WPF/MMT) based on nanofibrils of whey protein concentrate (WPC) together with MMT. Azo dyes' adsorption rate and the effect of contact time on adsorption were investigated for three adsorbents, *i.e.* whey protein polymer (WP), WP composite with MMT but without nanofibrils (WP/MMT), and WP composite combining amyloid nanofibrils and MMT (WPF/MMT). We studied the adsorption of eight azo dyes, including two cationic dyes (Chrysoidine-G and Bismarck brown-R), two reactive dyes (reactive black 5 and reactive orange 16), two acid dyes (acid red 88 and acid red 114), and also two direct dyes (direct violet 51 and Congo red) (see structures in **Supp. Table 1**). To gain a better insight into the adsorption process, the effects of dye concentration and adsorbent dose on Chrysoidine-G removal were examined using WPF/MMT nanocomposite, and finally, adsorption isotherms and kinetics of Chrysoidine-G were studied in detail.

2. Materials and Methods:

2.1. Materials

Whey Protein Concentrate 8010 (WPC with 80% protein) was obtained from Hilmar™ (North Lander Avenue, P.O. Box 910 Hilmar, CA). The montmorillonite K-10 (surface area 220-270 m^2/g), all 8 azo dyes (**Supp. Table 1**) and Thioflavin-T (ThT) were from Sigma-Aldrich (St. Louis, MO). Glycerol, all salts, and other materials were from Merck (Darmstadt, Germany).

2.2. Preparation of WPC Polymer and Nanocomposites

To prepare MMT suspensions, 6 g of MMT was added to 20 mL deionized water in a sealed beaker and was heated (~80°C) with continuous magnetic stirring for 1 h, followed by sonication for 30 min in an ultrasonic bath (JAC 2010 KODO, Gyeonggi-do, Korea) to disperse MMT. **Fig. 1** illustrates the key steps for the preparation of different whey protein-based polymer and composites, without nanofibrils (the black-arrows path), and with nanofibrils (the white-arrow path). In both pathways, nanocomposites are formed by adding 3% w/v of dispersed MMT to the film-forming solution before casting. At the first stage, 8% (w/v) of WPC was hydrated in deionized water using a magnetic stirrer, and centrifuged (13000 rpm, 30 min, at 4°C) to remove insoluble protein (Bolder, Hendrickx, Sagis, & van der Linden, 2006). To produce films without nanofibrils (WP and WP/MMT), the pH was adjusted

to 7 using NaOH (6M), glycerol (40% v/w WPC) was added, and the solution was stirred at 85°C for 30 min in a water bath. To produce films containing nanofibrils (WPF and WPF/MMT), the pH was adjusted to 2 using 12M HCl, and the solution stirred at 85°C for 4.5 h (Kawecka-Radomska et al., 2015; Mohammadian & Madadlou, 2016). During this step, sampling was performed to monitor the fibrillation process (see section 3.1.). The resulting solution was then cooled, and the pH was adjusted to 7. Subsequently glycerol (40% v/w WPC), and for the WPF/MMT nanocomposite, 3% dispersed MMT, were added, and the mixtures were stirred thoroughly before casting. Afterward, the cast solution was dried at 37°C overnight, followed by 2 h at 70°C. Finally, the films were immersed in distilled water at 4°C for 48 h to remove non-cross-linked parts (Škorić-Lučić, Stanojković, Milosavljević, & Kalagasidis-Krušić, 2018), and then dried at 100°C for 1 h.

3. Assessment of Nanofibril Formation

3.1. ThT Fluorescence Assay

We used ThT fluorescence to monitor the progress of fibrillation (Biancalana & Koide, 2010; Gade Malmos et al., 2017). At different times during fibrillation (**Fig. 1**), a 10 µL sample of the solution was added to 490 µL of 12 µM ThT solution in Tris buffer 10mM (pH 8). Subsequently, the fluorescence emission spectra of samples were recorded in the range of 450 to 550 nm with excitation at 440 nm (Varian Cary Eclipse fluorescence spectrophotometer, Australia). The excitation and emission slit widths were 5 and 10 nm, respectively.

3.2. Transmission Electron Microscopy (TEM)

After fibrillation and adjusting the pH to 7 (**Fig. 1**), 5 µL of the solution was placed onto a carbon-coated, glow-discharged 400-mesh grid for 30 s. The grid was stained with phosphotungstic acid 1% (pH 6.8) and blotted dry. Images were recorded on a TEM microscope (JEM-1010; JEOL, Tokyo, Japan) at 60 kV, using an Olympus KeenView G2 camera.

3.3. Material Characterization

3.3.1. Scanning Electron Microscopy (SEM)

The morphology of the surfaces and fracture (cross-section) surfaces of all films were visualized using SEM (VEGAII TESCAN, Czech Republic). To prepare the fracture surface, small pieces of the WP films were frozen by immersing in liquid nitrogen and then fractured manually. The surface and fracture sides of the films were mounted on the specimen stubs and then sputter-coated with a thin layer of gold and placed into the scanning electron microscope to observe the surface and cross-section morphology of the films.

3.3.2. Fourier-Transform Infrared (FT-IR) Spectroscopy

FT-IR spectra of the WPF/MMT, WP, and pristine MMT were recorded using a Perkin-Elmer Spectrum One spectrometer (Waltham, MA, USA) at the range of 400-4000 cm^{-1}. Powdered samples were mixed and ground with KBr powder to make packed tablets for FT-IR measurement.

3.3.3. X-ray Diffraction (XRD)

XRD measurements were performed on the WPF/MMT, WP, and pristine MMT using a Philips PW 1730 diffractometer (Eindhoven, The Netherlands), employing Cu Kα radiation source (λ= 1.54060 Å). The data were collected for 2θ values 0.71-9.99° in 0.02° step size, and 10.00-79.95 values in 0.05° step sizes.

3.3.4. Nitrogen Adsorption Isotherm (BET)

Nitrogen adsorption/desorption isotherms were measured with a BELSORP-miniII (Osaka, Japan) Brunauer-Emmett-Teller (BET) analyzer at 77 K. Before measurements, the nanocomposite samples were degassed at 180°C in a vacuum chamber for 8 h.

3.4. Batch Dye Adsorption Studies

We first investigated the decolorization percentage of WPF/MMT compared with WP, WP/MMT by immersing 2% w/v adsorbent in the dye solutions. The initial concentration of the dyes in distilled water was 250 mg/L. During the decolorization process, 200 µL of the dye solutions were collected at different times and their absorbance was measured using an EPOCH12 plate reader (BioTek, Winooski, Vermont, USA) at their maximum absorbance wavelength (**Supp. Table 1**). The percentage of decolorization (%) was calculated as follows:

$$Decolorization\ \% = \frac{(C_0 - C_t)}{C_0} \times 100 \quad (1)$$

where C_0 and C_t (mg/L) are the concentrations of the examined dyes at the beginning of the experiment and after time t, respectively.

To calculate the amount of dye adsorbed by the absorbent (*i.e.* q_t, in units of mg/g), different concentrations of Chrysoidine-G (25-250 mg/L) and adsorbent (1.45 – 17.3 g/L) were employed. The experiments were carried out in a reaction volume of 1.5 mL in 96-deep-well plates (Extragene, Taichung, Taiwan), which were covered with adhesive plate seals (Thermo scientific, USA), and put into an orbital shaker with 300 rpm speed (HOLDEKER5000D Orbital motion-UK) at 35°C. At different time intervals, the adsorption of solutions was measured. q_t was calculated as follows:

$$q_t = \frac{(C_0 - C_t)}{W} V \qquad (2)$$

where C_0 and C_t are the concentrations (in mg/L) of the examined dyes at the beginning and after time t, respectively, W is the weight of the adsorbent (g), and V is the volume of solution (L).

Equilibrium parameters for Chrysoidine-G adsorption, using different WPF/MMT dosages at 35°C, were analyzed using linear (Nernst), Longmuir, Freundlich, Temkin, and Dubinin-Radushkevich (D-R) Isotherm models:

Linear (Nernst) Isotherm:

The linear isotherm is the simplest adsorption isotherm, represented by the following equation:

$$q_e = K_{linear} C_e \quad (3)$$

where q_e (mg/g) is the amount of adsorbed dye at equilibrium, K_{linear} is the adsorption coefficient (Shamey & Zhao, 2014) (L/g) and C_e (mg/L) is the equilibrium concentration of free (not adsorbed) dye.

Langmuir Isotherm:

The Langmuir isotherm assumes monolayer formation and homogenous adsorption sites and can be represented by the following equation:

$$q_e = q_{max} \frac{K_L C_e}{1+K_L C_e} \quad (4)$$

where q_e (mg/g) is the amount of adsorbed dye at equilibrium, C_e (mg/L) is the equilibrium concentration dye, q_{max} (mg/g) is the maximum amount of adsorbed dye and K_L (L/mg) is the Langmuir constant related to the affinity of the surficial binding sites (Langmuir, 1918).

Freundlich Isotherm:

The Freundlich Isotherm equation is expressed as follows:

$$q_e = K_F C_e^{\frac{1}{n}} \quad (5)$$

where K_F (mg/g) and n are constants for the adsorbate (dye) and adsorbent (nanocomposite), respectively (Freundlich, 1907).

Temkin Isotherm:

The Temkin isotherm is expressed as follows (Temkin & Pyzhev, 1940):

$$q_e = \frac{RT}{b_T} lnA_T C_e \quad (6)$$

where R is the universal gas constant (8.314 $Jmol^{-1}K^{-1}$), T is the absolute temperature, b is a constant related to the heat of adsorption ($Jmol^{-1}$) and A_T is the Temkin isotherm constant (Lg^{-1}).

D-R Isotherm:

The D-R isotherm is given as follows (Ghaffari et al., 2017):

$$q_e = (q_m) exp(-\beta \varepsilon^2) \quad (7)$$

$$\varepsilon = RTln\left(1 + \frac{1}{C_e}\right) \quad (8)$$

where q_m (mg/g) is the D-R monolayer capacity, β is the sorption energy constant and ε is the Polanyi potential related to the equilibrium concentration and absolute temperature (T).

Kinetic models of adsorption were assessed using WPF/MMT nanocomposite (8 mg/L) and two different concentrations of Chrysoidine-G (50 and 100 mg/L). This experiment was carried out in 10 mL by incubating the samples in the orbital shaker (300 rpm) at 35℃ for 48 h. Then, the results were analyzed using pseudo-first-order, pseudo-second-order, and intra-particle diffusion kinetic models.

Pseudo-first-order

The linear form of the pseudo-first-order kinetic model (Lagergren, 1898) is generally expressed as follows:

$$ln(q_e - q_t) = lnq_e - k_1 t \quad (9)$$

where q_e and q_t (mg/g) are the amounts of the adsorbed dye at equilibrium and at the measured time respectively and k_1 is the pseudo-first-order rate constant (1/min) (Azizian, 2004).

Pseudo-second-order

The linearized form of the pseudo-second-order model (Ho & McKay, 1999) is expressed as:

$$\frac{t}{q_t} = \frac{1}{k_2 q_e^2} + \frac{t}{q_e} \quad (10)$$

where q_e and q_t (mg/g) are the amounts of adsorbed dye at equilibrium and at the time t (min), respectively while k_2 is the pseudo-second-order rate constant of sorption. The plot of t/q_t versus t gives a straight line in which q_e and k_2 could be calculated from the slope ($1/k_2q_e^2$) and intercept ($1/q_e$), respectively (Azizian, 2004).

Intra-particle diffusion

The intra-particle diffusion kinetic model (Weber & Morris, 1963) is used to investigate whether intra-particle diffusion is the rate-limiting step in the adsorption of Chrysoidine-G by WPF/MMT. The linear form of the intra-particle diffusion equation can be presented as:

$$q_t = k_i \times t^{\frac{1}{2}} + C_i \quad (11)$$

where k_i (mg/g $min^{1/2}$) is the intra-particle diffusion rate constant and C_i (mg/g) is the intercept of the plot related to the boundary layer influence (Hassani, Soltani, Karaca, & Khataee, 2015).

4. Results and Discussion:

4.1. Assessment of Nanofibril Formation

Amyloidogenic protein/ peptides, as implied in the name, can self-assemble into highly ordered nanofibrils under particular conditions. In accordance with previous studies (Kawecka-Radomska et al., 2015; Mohammadian & Madadlou, 2016), we fibrillated whey protein at pH 2 and 85°C and confirmed amyloid formation using the fluorescent amyloid reporter ThT along with TEM images (**Supp. Fig. 1**). ThT fluorescence is a common method to detect amyloid formation *in vitro* (Gade Malmos et al., 2017). Though not entirely quantitative, ThT fluorescence intensity is related to the overall mass of the formed fibrils (Biancalana & Koide, 2010). The increasing fluorescence intensity of ThT over time (**Supp. Fig. 1a**) suggested that WP was undergoing fibril formation. In addition, the presence of nanofibrils was confirmed by TEM images (**Supp. Fig. 1b**).

4.2. Materials Characterization

4.2.1. SEM Analysis

The microstructure and morphology of the produced materials were studied by SEM (**Fig. 2**). WP showed a rough and porous surface, while its cross-section is smooth and homogenous. In contrast, WPF (with nanofibrils) exhibited a rough and heterogenous cross-section. These morphologies might be related to the different viscosities of the film-forming solutions. WPF solution was highly viscous, allowing it to trap air bubbles and produce a porous cross-section. Nevertheless, the WPF surface was smooth and undulated because of clustered fibrils, similar to observations by Akkermans and coworkers (Akkermans et al., 2008). WP composites with MMT showed different morphologies on their upward and downward sides (in contact with air and the mold respectively) (**Fig. 2b1, b2**). The upward sides were rather similar to the surface of WP films (**Fig. 3a**); while the downward sides show a more rugged surface, in which MMT particles are visible. Interestingly, soaking in water increased porosity (**Fig. 2c**). WPF/MMT shows a homogenous cross-section. In remarkable contrast, the nanocomposite without nanofibrils (WP/MMT) exhibited a bilayer structure (**Fig. 2b and 3**). By comparing the composites' cross-sections, we conclude that nanofibrils contribute to the uniform dispersion of MMT particles in the WP matrix. We attribute the bilayer structure to phase separation between the WP and MMT components due to weak intermolecular forces between these two components. In contrast, the more viscous WPF solution can probably disperse MMT particles in the matrix thanks to nanofibrils crosslinking the individual MMT particles (see sketch in **Fig. 3**). While this bilayer structure has not been reported previously, the structures of WP, WPF, and WPF/MMT are similar to previous reports (Hosseinzadeh, Zoroufi, & Mahdavinia, 2015; Wakai & Almenar, 2015). The only exception is the work by Kumar et al., (2010) who observe that fracture images are undulated and similar to what we obtained using manually torn samples (**Supp. Fig. 2**) as opposed to fracturing in liquid nitrogen. They noted that "The white strands in the SEM images correspond to MMT platelets" (Kumar, Sandeep, Alavi, Truong, & Gorga, 2010a, 2010b). However, since these strands are present in our WP films too (*i.e.* in the absence of MMT) and we do not observe them in the N_2-fractured surface, we assume this structure to be caused by the glycerol plasticizer.

4.2.2. XRD Analysis

XRD is a common analysis method to verify composites' intercalated or exfoliated structures. The XRD pattern of WPF/MMT, WP and pristine MMT are shown in **Fig. 4a.** The XRD pattern of WP had only a broad peak around 20-22°, indicating a lack of crystallinity and amorphous shape, as confirmed in the macrostructure (Azevedo et al., 2015). When MMT was used as filler in the amorphous whey protein matrix, the composite exhibited very similar patterns to the pristine MMT, demonstrating a crystalline form of the composite, which is only modestly affected by the surrounding whey matrix. The XRD pattern of MMT exhibited one characteristic peak at 5.52°, representing the basal spacing of 1.60 nm, as is expected for calcium montmorillonite (Tong et al., 2018). For the WPF/MMT nanocomposite, the peak has shifted to 4.65° (*i.e.* a basal spacing of 1.90 nm) and has broadened, indicating that the whey protein matrix is intercalated into the MMT interlayer space, leading potentially to a higher degree of disorder.

4.2.3. FT-IR Spectroscopy

The functional groups of the prepared nanocomposite were investigated by FT-IR analysis (**Fig. 4b**). The main IR absorption of the protein backbone is related to amide bands in the 1700-1200 cm^{-1} region (Kong & Yu, 2007) which can all be detected in both WP and WPF/MMT spectra (right shaded area in **Fig. 4b**). Also, there are some peaks around 2800-3000 cm^{-1} which can be assigned to fats and oils (Andrade et al., 2019) in both WP and WPF/MMT spectra (left shaded area). Thus peaks between 2854 and 2923 are specific for dairy fatty acids. Furthermore, characteristic peaks of MMT (shown by grids) were observed in the composite too. As is listed in **Supp. Table 2**, WPF/MMT exhibited both MMT and WP main functional groups. However, in the composite, bands at 3697 and 3622 cm^{-1}, related to free OH vibration, were reduced in intensity, implying that there are less free OH bands in the nanocomposite. Some of the free hydroxyl groups found in MMT may have formed hydrogen bonds with the whey proteins (Shaabani, Sirousazar, & Kheiri, 2016). Furthermore, based on the FT-IR spectra of the WP/MMT and WPF/MMT presented in **Supp. Fig. 3** in the absence of nanofibrils, some peaks related to MMT and amide bands (shown by red and black stippled lines, respectively) are less intense, while changes in other peaks (indicated by arrows) show alterations in aluminosilicate functional groups. In contrast, amide band peaks around 1642, 1536 and 1448 cm^{-1} increased in intensity along with the peak around 3424 cm^{-1}, indicating more hydrogen bonding in this composite. Note that after soaking in water, the WP films do not show any of the typical peaks of glycerol (five peaks in region 800 cm^{-1} to 1150 cm^{-1}) (Wakai & Almenar, 2015). This means that glycerol has been removed from during soaking in water.

4.2.4. BET Analysis

BET analysis is a common technique for determining the surface area, possible adsorption mechanism and pore shape of the porous materials, through measurement of the amount of N_2 adsorption/desorption at 77 K (Thommes et al., 2015). The N_2 sorption isotherm of WPF/MMT nanocomposite (**Fig. 5a**) curves upwards with increasing pressure and does not show a point B (*i.e.* a knee on the isotherm) which would otherwise indicate complete monolayer coverage. Therefore there is no recognizable monolayer formation. Moreover, the value of the C parameter (1.74) is below 2. These observations all indicate that the isotherm is type III, in which the interaction between adsorption and adsorbate is relatively weak, and the adsorbed molecules are clustered around favorable sites (Sing, 1985; Thommes et al., 2015). The sorption isotherm showed a hysteresis loop which according to IUPAC nomenclature can be classified as Type H3 (no adsorption limit at high p/p_0) which is in line with other clay composites (Abu-Danso et al., 2020; Tong et al., 2018).type H3 loop is commonly seen in non-rigid combinations of plate-like particles (*e.g.*, clays) (Thommes, 2010; Thommes et al., 2015). The specific surface area and pore radius were determined by the BJH method (**Fig. 5b**) to be 1.28 m^2/g and 2.13 nm, respectively. It should be noted that H3 hysteresis loop does not generally provide a reliable estimate of the pore size distribution (Sing, 1985; Tong et al., 2018). Besides, the nanocomposite sample used for the BET test was in flakes, not in powder form. The surface area of the composite is very modest in comparison with pristine MMT (220-270 m^2/g), bentonite micropowder (67 m^2/g) (Bulut, Akçay, Elma, & Serhatlı, 2009), or similar composites *e.g.* clay-cellulose composite (31.16 m^2/g) (Abu-Danso et al., 2020), *Moringa oleifera*

seed protein-montmorillonite composite (4.90 m^2/g) (Mi et al., 2019) or carbon/montmorillonite nanocomposite (39.5 m^2/g) (Tong et al., 2018).

4.3. Batch Dye Adsorption Studies

4.3.1. Decolorization Rate of Some Different Classes of Azo Dyes

The decolorization capability of WPF/MMT nanocomposite was examined using the eight azo dyes mentioned in **Supp. Table 1**. Cationic dyes (Chrysoidine-G and Bismarck brown-R) adsorbed much faster than the other dyes (**Fig. 6a**). Most likely the negative charge of MMT helps adsorb the cationic dyes via ion exchange and electrostatic interactions. As regards acidic dyes, acid red 88 adsorbed faster (89% after 4 days) than acid red 114 (80% after 7days), which we ascribe to its smaller molecular structure (**Fig. 6b**). Congo red and direct violet 51 presented highly similar patterns in their adsorption timeline; both are ~80% absorbed after 4 days but have not reached a plateau after a week (**Fig. 6c**). Finally, reactive dyes (reactive black 5 and reactive orange 16) adsorbed more slowly than the other dyes and required more time to reach equilibrium (**Fig. 6d**).

The decolorization timeline using WP and WP/MMT nanocomposite is presented in **Supp. Fig. 4**. In the first days, these two nanocomposites adsorbed Congo red, direct violet and acid red 88 dyes significantly faster than WPF/MMT. However, over longer time scale, the extent of absorption on WP and WP/MMT decreased slightly for some dyes (*i.e.* acid red 88, direct violet 51, reactive orange and reactive black). We observed that WP and WP/MMT were not as stable as WPF/MMT over a week of incubation with the dyes. Also, they become more swollen than the amyloid-containing composite, WPF/MMT (**Fig. 7**). Swelling depends on the solvent and the cross-link density (Cowie & Arrighi, 2007; Khaleghi, Ahmadi, Shahraki, Aliakbari, & Morshedi, 2020). Thus, in the presence of nanofibrils the composite is more cross-linked, and hence reinforces the nanocomposite (Akkermans et al., 2008), making it more stable in different dye solutions. We note that to achieve this stability, drying the nanocomposite in 100 ℃, for 1 h (the last stage in **Fig. 1**) is necessary as heat treatment to form enough cross-link between nanofibrils and MMT components (see sketch in **Fig. 3** and **Fig. 7d**).

4.3.2. Effect of Initial Dye Concentration

We decided to carry out a more detailed analysis of the absorption process using the cationic dye Chrysoidine-G, which showed the fastest and most extensive level of absorption. **Fig. 8a** shows the influence of the different initial dye concentrations (from 25 to 250 mg/L) and contact time on Chrysoidine-G dye removal, using WPF/MMT (8 g/L). Although the rate of adsorption (*i.e.* the plot slope) decreased slightly with increasing initial concentration (**Fig. 8a**), the equilibrium adsorption percentage did not change very much, and WPF/MMT was able to adsorb more than 93% of the dye at all concentrations over a 24-h period. In contrast, for most adsorbents, a decrease in adsorption percentage has been reported with increasing initial dye concentration (Jiang, Dinh, & Hsieh, 2017; P. S. Kumar et al., 2010; M. Kamil, H. Abdalrazak, F. Halbus, & H. Hussein, 2014); moreover, the amount of the adsorbed dye (q_t,) is proportional to the increase in initial dye concentration, as when the initial dye concentration was doubled, q_t was doubled too ($R^2 \geq 0.9997$) (**Fig. 8a, upper inset graph**). Thus, the similar relative absorption at different dye concentrations indicates that the only limiting factor, in this adsorption dose, is bulk diffusion of dye molecules from the solution to the

boundary layer on the adsorbent surface (Weber & Morris, 1963). These results are consistent with the results of BET, isotherms, and kinetics studies (see below), which indicate the existence of an unlimited number of adsorption sites under the present conditions (*i.e.* we do not reach the full capacity of adsorption under our experimental conditions).

4.3.3. Effect of Adsorbent Dose

The optimum WPF/MMT dose for adsorbing Chrysoidine-G dye (100 mg/L) was investigated using different WPF/MMT doses over a week (**Fig. 8b).** Increasing the WPF/MMT dose from 1.45 to 5.8 g/L increased decolorization rate; however, further dose increase does not significantly affect either decolorization or q_e. Therefore, approximately 9 g/L is the optimum adsorbent dosage for the adsorption of Chrysoidine-G by WPF/MMT. As using the adsorbent below this critical amount, the adsorption cannot proceed effectively. These results are in agreement with the study of Namasivayam and Kavitha (2002) for Congo red adsorption by coir pit carbon (Namasivayam & Kavitha, 2002).

4.4. Adsorption Isotherms

Adsorption isotherms studies provide useful information on how solutes interact with adsorbents, and it is essential in optimizing the use of adsorbents. In this study, equilibrium adsorption parameters of Chrysoidine-G adsorption onto WPF/MMT were investigated at 35℃ using different adsorbent dosages and subsequently fitted with linear (Nernst), Longmuir, Freundlich, Temkin, and D-R Isotherm models.

The equilibrium absorption data showed a simple linear relationship between the total and absorbed amount of dye (**Fig. 9a**). Similarly, the best-fitted curves (R^2>989) obtained using the equations describing Langmuir, Freundlich, and Temkin isotherms were all precisely linear (**Fig. 9a** and summarized in **Table 1**), making it impossible to distinguish between them. Accordingly, the simplest possible equation (with the least number of parameters) should be selected, *i.e.* the simple linear isotherm. In a model with a linear isotherm (C-class), the number of adsorption sites remains constant until saturation of the adsorbent. This means that the adsorption surface increases during the adsorption process, and can be considered as an unlimited number of adsorption sites because as soon as each molecule is adsorbed, a new vacant site is generated. **Fig. 9b** illustrates the conditions of this C-class system; the adsorbed molecules penetrate the inner layers of adsorbent, and since the entrance of pores is not occupied, the adsorption process proceeds continuously (Giles, Smith, & Huitson, 1974). A microscopic look at the boundary layer of WPF/MMT (**Fig. 9c**), reveals that the adsorbent surface in the solution exhibited a gel-like surface where dye molecules can penetrate, and aggregate in some, probably more favorable, places, as indicated with black arrows in the picture. Thus, the process proceeds continuously. This conforms to the BET results in section 4.2.4 which follows the type III isotherm model, indicating that the adsorbed molecules are clustered around favorable sites, and the adsorption process can proceed continuously.

358 **Table 1:** Comparison between linear and non-linear forms of adsorption isotherms for Chrysoidine-G onto WPF/MMT at 35°C

	Linear (Nernst)	Langmuir	Freundlich	Temkin	D-R
Non-linear form	0.98982	0.98999	0.98982	0.98997	0.894517
Linear form	0.9887	0.0534	0.92	0.9485	0.8615

359 To gain a better insight into the adsorption mechanism, we also studied the linearized versions of
360 the adsorption isotherms (**Supp. Fig. 5**). Comparing the related R^2 amounts of these two forms
361 (**Table 1**), it is noticeable that despite high conformity with the Langmuir model in the non-linear
362 form, the adsorption process does not follow the Langmuir isotherm well in the linear form. This
363 agrees with the BET results (**Fig. 5a**) which shows no completion of monolayer adsorption.

364 4.5. Kinetics of Adsorption

365 To study the efficiency and the mechanism of adsorption, the kinetics of adsorption of Chrysoidine-G
366 onto WPF/MMT were analyzed using pseudo-first-order, pseudo-second-order and intra-particle
367 diffusion models based on the raw adsorption data presented in **Fig. 10a**.

368 **Pseudo-first-order**

369 The pseudo-first-order parameters for the adsorption using WPF/MMT are listed in **Table 2**. It is
370 clear from **Fig. 10b**, that the pseudo-first-order equation provides an extremely poor fit to the data.
371 Furthermore, the calculated q_e is not in agreement with the experimental q_e. We conclude that
372 experimental data is not fitted well with this model.

373 **Pseudo-second-order**

374 The pseudo-second-order parameters are presented in **Table 2**. Clearly this leads to a much better fit
375 than the pseudo-first-order results as well as a very good agreement between experimental (*i.e.*
376 measured directly from the experiment) and calculated q_e (*i.e.* calculated from the plot slope (**Fig.**
377 **10c**), eq. 10), making it clear that this is an excellent model for Chrysoidine-G adsorption. As a
378 corollary, this implies that chemisorption is the rate-limiting step of Chrysoidine-G adsorption using
379 WPF/MMT (Ho & McKay, 1999). Also, it can be observed that the value of the rate constant k_2 is
380 halved when the initial dye concentration is doubled. Thus Chrysoidine-G adsorption on WPF/MMT
381 depends only on diffusion and is not limited by the amount of adsorbent, indicating the presence of
382 infinite adsorption sites. This is in agreement with the results of our adsorption isotherms study in
383 section 4.4 which has been mentioned that the adsorption of each molecule generates a new free
384 site (**Fig. 9b**); therefore, it can be considered as increasing or infinitive adsorption sites.

385 **Intra-particle diffusion**

386 The intra-particle diffusion parameters are shown in **Table 2**. As shown in **Fig. 10d**, the intra-particle
387 diffusion curve (adsorption versus square root of time, eq. 11) shows three linear regions, revealing
388 three stages in the adsorption process. A similar three-stage plot has been reported on adsorption of
389 malachite green dye by cellulose nanofibril aerogel (Jiang et al., 2017), or chitin hydrogels (Tang,
390 Zhou, & Zhang, 2012), adsorption of multi-azo dye using chitosan-starch hydrogel (Ngwabebhoh,
391 Gazi, & Oladipo, 2016), and Congo red adsorption by cashew nutshell (P. S. Kumar et al., 2010).
392 According to the interpretation of this three-stage process (Jiang et al., 2017; Lee, Lee, Chia, Tan, &

Gan, 2014; Ngwabebhoh et al., 2016; Tang et al., 2012), the first stage (up to 60 minutes, 70% adsorption) is related to the diffusion of dye molecules from the bulk solution to the external surface of WPF/MMT. The second stage (up to 5 h, ~90% adsorption) can be attributed to intra-particle diffusion of dye molecules into the interior of WPF/MMT, and finally, the third linear stage is related to the equilibrium phase of the adsorption process and reflects the decrease in dye concentration (AGARRY & OGUNLEYE, 2014; Tang et al., 2012). Thus, it can be concluded that the adsorption data can be described with the intra-particle diffusion model. The constant C_i, which is related to the boundary layer thickness, increases when the dye concentration increases. Indicating an increase in the thickness of boundary layer with increasing the initial concentration, therefore the rule of surface sorption becomes more important as the rate-limiting step (P. S. Kumar et al., 2010).

Table 2: Kinetic parameters for Chrysoidine-G adsorption onto WPF/MMT (8 mg/L) at 35°C over 48 h

		Pseudo-first-order			Pseudo-second-order			Intra-particle diffusion		
C_0 (mg/L)	q_e(exp) (mg/g)	K_1 (1/min)	q_e(cal) (mg/g)	R^2	K_2 (g/mg min)	q_e(cal) (mg/g)	R^2	K_i (mg/g $min^{1/2}$)	C_i (mg/g)	R^2
50	**5.67**	-0.0032	1.55	0.8603	0.0105	5.77	0.9997	0.0925	3.9618	0.9855
100	**11.26**	-0.0033	3.03	0.8688	0.0053	11.45	0.9999	0.1573	8.1985	0.9807

Most of our experiments were performed in a small volume (1.5 mL). To test for possible scale-ups, the kinetic experiment performed on a larger scale of 10 mL (**Fig. 10a**). Comparison of the results of adsorption of Chrysoidine-G (100 mg/L) using 8 g/L of WPF/MMT shows that the decolorization percentage and q_t values are very close in both volumes; this suggests that the adsorption process may be scaled up without significant changes in the results.

5. Conclusions

In this study, a novel bio-nanocomposite was developed from WPC using proteinaceous nanofibrils together with MMT (WPF/MMT). The structure of the resulted nanocomposite was characterized using SEM, FT-IR, BET, and XRD methods, which indicated WPF/MMT is a nanocomposite with intercalated and exfoliated structure. Investigating the adsorption efficacy for the different classes of azo dyes with different physicochemical properties revealed that WP, WP/MMT and WPF/MMT can be used to adsorb a wide range of azo dyes. WPF/MMT presented a better performance in adsorbing cationic dye. Although WP and WP/MMT adsorbed acid, direct and reactive dyes more rapidly than WPF/MMT, only WPF/MMT remained stable in all studies for a long time, probably because of the presence of nanofibrils, higher cross-link density and lower swelling capacity. In further studies on the decolorization process, it was determined that the adsorption phenomenon was almost independent of the dye concentration, and the optimum adsorbent dosage was ~9 g/L. To decipher the mechanism underlying the adsorption process, different isotherm and kinetic models were investigated. Since kinetic data could be fitted very well using a pseudo-second-order model, we conclude that chemisorption plays a rate-limiting role in the adsorption process.

Moreover, comparing linear and non-linear forms of adsorption isotherms suggests that the process is mostly fitted with the linear (Nernst) isotherm model, indicating the existence of unlimited absorption sites, which in turn conforms with the results of BET (Type III isotherm), kinetic studies (both pseudo-second-order and intra-particle diffusion), and also optical microscopy. Overall, whey protein-based polymer and nanocomposites have clear potential as effective adsorbents for different classes of dyes or even other pollutants from wastewater.

Acknowledgments

This work was supported by the National Institute of Genetic Engineering and Biotechnology. The authors acknowledge Bioprocess Engineering department, Institute of Industrial and Environmental Biotechnology, National Institute of Genetic Engineering and Biotechnology, Tehran, Iran. D.E.O. is grateful for support from the Independent Research Foundation Denmark | Natural Sciences (grant no. 8021-00208B). The authors would like to thank Farhang Aliakbari for helpful discussions, and Zahra Najarzadeh for help with TEM images. Tayebe Bagheri Lotfabad is acknowledged for helpful suggestions in the film preparation process.

Conflict of interest

The authors declare that they have no conflicts of interest.

References

Abu-Danso, E., Peräniemi, S., Leiviskä, T., Kim, T., Tripathi, K. M., & Bhatnagar, A. (2020). Synthesis of clay-cellulose biocomposite for the removal of toxic metal ions from aqueous medium. *Journal of hazardous materials, 381*, 120871. doi:https://doi.org/10.1016/j.jhazmat.2019.120871

Adeyemo, A. A., Adeoye, I. O., & Bello, O. S. (2017). Adsorption of dyes using different types of clay: a review. *Applied Water Science, 7*(2), 543-568. doi:10.1007/s13201-015-0322-y

AGARRY, S., & OGUNLEYE, O. J. T. (2014). Chemically treated kola nut pod as low-cost natural adsorbent for the removal of 2, 4-dinitrophenol from synthetic wastewater: batch equilibrium, kinetic, and thermodynamic modelling studies. *Journal of Engineering Environmental Sciences, 38*(1), 11-40.

Akkermans, C., Van der Goot, A. J., Venema, P., Van der Linden, E., & Boom, R. M. (2008). Properties of protein fibrils in whey protein isolate solutions: Microstructure, flow behaviour and gelation. *International dairy journal, 18*(10-11), 1034-1042. doi:https://doi.org/10.1016/j.idairyj.2008.05.006

Andrade, J., Pereira, C. G., Almeida Junior, J. C. d., Viana, C. C. R., Neves, L. N. d. O., Silva, P. H. F. d., . . . Anjos, V. d. C. d. (2019). FTIR-ATR determination of protein content to evaluate whey protein concentrate adulteration. *LWT, 99*, 166-172. doi:https://doi.org/10.1016/j.lwt.2018.09.079

Azevedo, V. M., Dias, M. V., Borges, S. V., Costa, A. L. R., Silva, E. K., Medeiros, É. A. A., & Soares, N. d. F. F. (2015). Development of whey protein isolate bio-nanocomposites: Effect of montmorillonite and citric acid on structural, thermal, morphological and mechanical properties. *Food Hydrocolloids, 48*, 179-188. doi:https://doi.org/10.1016/j.foodhyd.2015.02.014

Azizian, S. (2004). Kinetic models of sorption: a theoretical analysis. *Colloid Interface Science, 276*(1), 47-52. doi:https://doi.org/10.1016/j.jcis.2004.03.048

Biancalana, M., & Koide, S. (2010). Molecular mechanism of Thioflavin-T binding to amyloid fibrils. *Biochimica et Biophysica Acta -Proteins Proteomics, 1804*(7), 1405-1412. doi:https://doi.org/10.1016/j.bbapap.2010.04.001

Bolder, S. G., Hendrickx, H., Sagis, L. M., & van der Linden, E. (2006). Fibril assemblies in aqueous whey protein mixtures. *Journal of agricultural and food chemistry, 54*(12), 4229-4234. doi:https://doi.org/10.1021/jf060606s

Bolisetty, S., Reinhold, N., Zeder, C., Orozco, M. N., & Mezzenga, R. (2017). Efficient purification of arsenic-contaminated water using amyloid–carbon hybrid membranes. *Chemical Communications, 53*(42), 5714-5717. doi:https://doi.org/10.1039/C7CC00406K

Bulut, Y., Akçay, G., Elma, D., & Serhatlı, I. E. (2009). Synthesis of clay-based superabsorbent composite and its sorption capability. *Journal of hazardous materials, 171*(1-3), 717-723. doi:https://doi.org/10.1016/j.jhazmat.2009.06.067

Cherny, I., & Gazit, E. (2008). Amyloids: not only pathological agents but also ordered nanomaterials. *Angewandte Chemie International Edition, 47*(22), 4062-4069. doi: https://doi.org/10.1002/anie.200703133

Cowie, J. M. G., & Arrighi, V. (2007). *Polymers: chemistry and physics of modern materials*: CRC press.

Farjami, T., Madadlou, A., & Labbafi, M. (2015). Characteristics of the bulk hydrogels made of the citric acid cross-linked whey protein microgels. *Food Hydrocolloids, 50*, 159-165. doi:https://doi.org/10.1016/j.foodhyd.2015.04.011

Fernández, C., Larrechi, M. S., & Callao, M. P. (2010). An analytical overview of processes for removing organic dyes from wastewater effluents. *TrAC Trends in Analytical Chemistry, 29*(10), 1202-1211. doi:https://doi.org/10.1016/j.trac.2010.07.011

Forgacs, E., Cserhati, T., & Oros, G. (2004). Removal of synthetic dyes from wastewaters: a review. *Environment international, 30*(7), 953-971. doi:https://doi.org/10.1016/j.envint.2004.02.001

Freundlich, H. (1907). Über die Adsorption in Lösungen. *Zeitschrift für physikalische Chemie, 57U*(1), 385-470. doi:https://doi.org/10.1515/zpch-1907-5723

Gade Malmos, K., Blancas-Mejia, L. M., Weber, B., Buchner, J., Ramirez-Alvarado, M., Naiki, H., & Otzen, D. (2017). ThT 101: a primer on the use of thioflavin T to investigate amyloid formation. *Amyloid, 24*(1), 1-16. doi:https://doi.org/10.1021/bi00041a047

Ghaffari, H., Pasalari, H., Tajvar, A., Dindarloo, K., Goudarzi, B., Alipour, V., & Ghanbarneajd, A. (2017). Linear and nonlinear two-parameter adsorption isotherm modeling: a case-study. *Int. J. Eng. Sci., 6*(9), 01-11. doi:10.9790/1813-0609010111

Ghosh, B. K., Hazra, S., Naik, B., & Ghosh, N. N. (2015). Preparation of Cu nanoparticle loaded SBA-15 and their excellent catalytic activity in reduction of variety of dyes. *Powder technology, 269*, 371-378. doi:https://doi.org/10.1016/j.powtec.2014.09.027

Giles, C. H., Smith, D., & Huitson, A. (1974). A general treatment and classification of the solute adsorption isotherm. I. Theoretical. *Journal of colloid interface science, 47*(3), 755-765. doi:https://doi.org/10.1016/0021-9797(74)90252-5

Han, H., Rafiq, M. K., Zhou, T., Xu, R., Mašek, O., & Li, X. (2019). A critical review of clay-based composites with enhanced adsorption performance for metal and organic pollutants. *Journal of hazardous materials, 369*, 780-796. doi:https://doi.org/10.1016/j.jhazmat.2019.02.003

Hassani, A., Soltani, R. D. C., Karaca, S., & Khataee, A. (2015). Preparation of montmorillonite–alginate nanobiocomposite for adsorption of a textile dye in aqueous phase: isotherm, kinetic and experimental design approaches. *Journal of Industrial Engineering Chemistry, 21*, 1197-1207. doi:https://doi.org/10.1016/j.jiec.2014.05.034

Ho, Y.-S., & McKay, G. (1999). Pseudo-second order model for sorption processes. *Process biochemistry, 34*(5), 451-465. doi:https://doi.org/10.1016/S0032-9592(98)00112-5

Hosseinzadeh, H., Zoroufi, S., & Mahdavinia, G. R. (2015). Study on adsorption of cationic dye on novel kappa-carrageenan/poly (vinyl alcohol)/montmorillonite nanocomposite hydrogels. *Polymer Bulletin, 72*(6), 1339-1363. doi:10.1007/s00289-015-1340-5

Jiang, F., Dinh, D. M., & Hsieh, Y.-L. (2017). Adsorption and desorption of cationic malachite green dye on cellulose nanofibril aerogels. *Carbohydrate Polymers, 173*, 286-294. doi:https://doi.org/10.1016/j.carbpol.2017.05.097

Jung, J. P., Gasiorowski, J. Z., & Collier, J. H. (2010). Fibrillar peptide gels in biotechnology and biomedicine. *Biomolecules, 94*(1), 49-59. doi:10.1002/bip.21326

Katheresan, V., Kansedo, J., & Lau, S. Y. (2018). Efficiency of various recent wastewater dye removal methods: A review. *Journal of environmental chemical engineering*.

Kausar, A., Iqbal, M., Javed, A., Aftab, K., Bhatti, H. N., & Nouren, S. (2018). Dyes adsorption using clay and modified clay: A review. *Journal of Molecular Liquids, 256*, 395-407. doi:https://doi.org/10.1016/j.molliq.2018.02.034

Kawecka-Radomska, M., Tomczyńska-Mleko, M., Wesołowska-Trojanowska, M., Kowalczyk, K., Chrząstek, M., & Mleko, S. (2015). Hard biodegradable biopolymer obtained from whey protein concentrate and montmorillonite. *Journal of Polymers the Environment, 23*(4), 534-540. doi:10.1007/s10924-015-0722-y

Khaleghi, M., Ahmadi, E., Shahraki, M. K., Aliakbari, F., & Morshedi, D. (2020). Temperature-dependent formulation of a hydrogel based on Hyaluronic acid-polydimethylsiloxane for biomedical applications. *Heliyon, 6*(3), e03494. doi:https://doi.org/10.1016/j.heliyon.2020.e03494

Kong, J., & Yu, S. (2007). Fourier transform infrared spectroscopic analysis of protein secondary structures. *Acta biochimica et biophysica Sinica, 39*(8), 549-559. doi:https://doi.org/10.1111/j.1745-7270.2007.00320.x

Kumar, P., Sandeep, K., Alavi, S., Truong, V., & Gorga, R. (2010a). Effect of type and content of modified montmorillonite on the structure and properties of bio-nanocomposite films based

on soy protein isolate and montmorillonite. *Journal of Food Science, 75*(5), N46-N56. doi:10.1111/j.1750-3841.2010.01633.x

Kumar, P., Sandeep, K., Alavi, S., Truong, V., & Gorga, R. (2010b). Preparation and characterization of bio-nanocomposite films based on soy protein isolate and montmorillonite using melt extrusion. *Journal of Food Engineering, 100*(3), 480-489. doi:https://doi.org/10.1016/j.jfoodeng.2010.04.035

Kumar, P. S., Ramalingam, S., Senthamarai, C., Niranjanaa, M., Vijayalakshmi, P., & Sivanesan, S. (2010). Adsorption of dye from aqueous solution by cashew nut shell: Studies on equilibrium isotherm, kinetics and thermodynamics of interactions. *Desalination, 261*(1-2), 52-60. doi:https://doi.org/10.1016/j.desal.2010.05.032

Lagergren, S. K. (1898). About the theory of so-called adsorption of soluble substances. *Sven. Vetenskapsakad. Handingarl, 24*, 1-39.

Langmuir, I. (1918). The adsorption of gases on plane surfaces of glass, mica and platinum. *Journal of the American Chemical society, 40*(9), 1361-1403. doi:https://doi.org/10.1021/ja02242a004

Lee, L., Lee, X., Chia, P., Tan, K., & Gan, S. (2014). Utilisation of Cymbopogon citratus (lemon grass) as biosorbent for the sequestration of nickel ions from aqueous solution: Equilibrium, kinetic, thermodynamics and mechanism studies. *Journal of the Taiwan Institute of Chemical Engineers, 45*(4), 1764-1772. doi:https://doi.org/10.1016/j.jtice.2014.02.002

Leung, W.-H., Lo, W.-H., & Chan, P.-H. (2015). Amyloid Fibrils as Rapid and Efficient Nano-biosorbents for Removal of Dye Pollutants. *RSC advances, 5*(109), 90022-90030. doi:10.1039/C5RA17182B

Lucas, M. S., Algarra, M., Jiménez-Jiménez, J., Rodríguez-Castellón, E., & Peres, J. A. (2013). Catalytic Activity of Porous Phosphate Heterostructures-Fe towards Reactive Black 5 Degradation. *International Journal of Photoenergy, 2013*, 1-6. doi:https://doi.org/10.1155/2013/658231

M. Kamil, A., H. Abdalrazak, F., F. Halbus, A., & H. Hussein, F. (2014). Adsorption of Bismarck Brown R Dye Onto Multiwall Carbon Nanotubes. *Journal of Environmental Analytical Chemistry, 01*(01), 2. doi:10.4172/2380-2391.1000104

Markandeya, Dhiman, N., Shukla, S. P., & Kisku, G. C. (2017). Statistical optimization of process parameters for removal of dyes from wastewater on chitosan cenospheres nanocomposite using response surface methodology. *Journal of Cleaner Production, 149*, 597-606. doi:https://doi.org/10.1016/j.jclepro.2017.02.078

Mi, X., Shang, Z., Du, C., Li, G., Su, T., Chang, X., . . . Tie, J. (2019). Adsorption of an Anionic Azo Dye Using Moringa oleifera Seed Protein-Montmorillonite Composite. *Journal of Chemistry, 2019*, 1-8. doi:https://doi.org/10.1155/2019/8464815

Mittal, V. (2009). Polymer layered silicate nanocomposites: a review. *materials, 2*(3), 992-1057. doi:10.3390/ma2030992

Mohammadian, M., & Madadlou, A. (2016). Characterization of fibrillated antioxidant whey protein hydrolysate and comparison with fibrillated protein solution. *Food Hydrocolloids, 52*, 221-230. doi:https://doi.org/10.1016/j.foodhyd.2015.06.022

Morshedi, D., Mohammadi, Z., Boojar, M. M. A., & Aliakbari, F. (2013). Using protein nanofibrils to remove azo dyes from aqueous solution by the coagulation process. *Colloids and Surfaces B: Biointerfaces, 112*, 245-254. doi:https://doi.org/10.1016/j.colsurfb.2013.08.004

Mukhopadhyay, R., Bhaduri, D., Sarkar, B., Rusmin, R., Hou, D., Khanam, R., . . . Bhatnagar, A. (2020). Clay–polymer nanocomposites: Progress and challenges for use in sustainable water treatment. *Journal of hazardous materials, 383*, 121125. doi:https://doi.org/10.1016/j.jhazmat.2019.121125

Namasivayam, C., & Kavitha, D. (2002). Removal of Congo Red from water by adsorption onto activated carbon prepared from coir pith, an agricultural solid waste. *Dyes and pigments, 54*(1), 47-58. doi:https://doi.org/10.1016/S0143-7208(02)00025-6

Nawaz, M. S., & Ahsan, M. (2014). Comparison of physico-chemical, advanced oxidation and biological techniques for the textile wastewater treatment. *Alexandria Engineering Journal, 53*(3), 717-722. doi:https://doi.org/10.1016/j.aej.2014.06.007

Ngwabebhoh, F. A., Gazi, M., & Oladipo, A. A. (2016). Adsorptive removal of multi-azo dye from aqueous phase using a semi-IPN superabsorbent chitosan-starch hydrogel. *Chemical Engineering Research and Design, 112*, 274-288. doi:https://doi.org/10.1016/j.cherd.2016.06.023

Palmieri, N., Forleo, M. B., & Salimei, E. (2017). Environmental impacts of a dairy cheese chain including whey feeding: An Italian case study. *Journal of Cleaner Production, 140*, 881-889. doi:https://doi.org/10.1016/j.jclepro.2016.06.185

Pandey, N., Shukla, S., & Singh, N. (2017). Water purification by polymer nanocomposites: an overview. *Nanocomposites, 3*(2), 47-66. doi:https://doi.org/10.1080/20550324.2017.1329983

Prazeres, A. R., Carvalho, F., & Rivas, J. (2012). Cheese whey management: A review. *Journal of environmental management, 110*, 48-68. doi:https://doi.org/10.1016/j.jenvman.2012.05.018

Şengil, İ. A., & Özacar, M. (2009). The decolorization of CI Reactive Black 5 in aqueous solution by electrocoagulation using sacrificial iron electrodes. *Journal of hazardous materials, 161*(2), 1369-1376. doi:https://doi.org/10.1016/j.jhazmat.2008.04.100

Shaabani, Y., Sirousazar, M., & Kheiri, F. (2016). Crosslinked swellable clay/egg white bionanocomposites. *Applied Clay Science, 126*, 287-296. doi:https://doi.org/10.1016/j.clay.2016.03.027

Shamey, R., & Zhao, X. (2014). *Modelling, simulation and control of the dyeing process*: Elsevier.

Sing, K. S. D. H. E., R. A. W. Haul, L. Moscou, R. A. Pierotti, J. Rouquerol, T. Siemieniewska. (1985). Reporting physisorption data for gas/solid systems with special reference to the determination of surface area and porosity (Recommendations 1984). *Pure and applied chemistry, 57*(4), 603-619. doi:https://doi.org/10.1351/pac198557040603

Škorić-Lučić, M. L., Stanojković, L. S., Milosavljević, N. B., & Kalagasidis-Krušić, M. T. (2018). Sorption of textile dyes from textile wastewater by chitosan-based hydrogel. *Tehnika, 73*(1), 11-18. doi:10.5937/TEHNIKA1801009L

Tang, H., Zhou, W., & Zhang, L. (2012). Adsorption isotherms and kinetics studies of malachite green on chitin hydrogels. *Journal of hazardous materials, 209-210*, 218-225. doi:https://doi.org/10.1016/j.jhazmat.2012.01.010

Temkin, M., & Pyzhev, V. (1940). Recent modifications to Langmuir isotherms. Retrieved from https://www.semanticscholar.org/paper/Recent-modifications-to-Langmuir-isotherms-Temkin-Pyzhev/1134555b00ec87bc3580a73d436b7a269e9f58fc

Thommes, M. (2010). Physical Adsorption Characterization of Nanoporous Materials. *Chemie Ingenieur Technik, 82*(7), 1059-1073. doi:https://doi.org/10.1007/s10450-014-9606-z

Thommes, M., Kaneko, K., Neimark, A. V., Olivier, J. P., Rodriguez-Reinoso, F., Rouquerol, J., & Sing, K. S. (2015). Physisorption of gases, with special reference to the evaluation of surface area and pore size distribution (IUPAC Technical Report). *Pure Applied Chemistry, 87*(9-10), 1051-1069. doi:https://doi.org/10.1515/pac-2014-1117

Tong, D. S., Wu, C. W., Adebajo, M. O., Jin, G. C., Yu, W. H., Ji, S. F., & Zhou, C. H. (2018). Adsorption of methylene blue from aqueous solution onto porous cellulose-derived carbon/montmorillonite nanocomposites. *Applied Clay Science, 161*, 256-264. doi:https://doi.org/10.1016/j.clay.2018.02.017

Vandevivere, P. C., Bianchi, R., & Verstraete, W. (1998). Treatment and Reuse of Wastewater from the Textile Wet-Processing Industry: Review of Emerging Technologies. *Journal of Chemical Technology and Biotechnology, 72*(4), 289-302. doi:https://doi.org/10.1002/(SICI)1097-4660(199808)72:4<289::AID-JCTB905>3.0.CO;2-%23

Wakai, M., & Almenar, E. (2015). Effect of the presence of montmorillonite on the solubility of whey protein isolate films in food model systems with different compositions and pH. *Food Hydrocolloids, 43*, 612-621. doi:https://doi.org/10.1016/j.foodhyd.2014.07.022

Weber, W. J., & Morris, J. C. (1963). Kinetics of adsorption on carbon from solution. *Journal of the Sanitary Engineering Division, 89*(2), 31-60. Retrieved from https://cedb.asce.org/CEDBsearch/record.jsp?dockey=0013042

Weng, C.-H., Lin, Y.-T., & Yuan, H.-M. (2013). Rapid decoloration of Reactive Black 5 by an advanced Fenton process in conjunction with ultrasound. *Separation and Purification Technology, 117*, 75-82. doi:https://doi.org/10.1016/j.seppur.2013.03.047

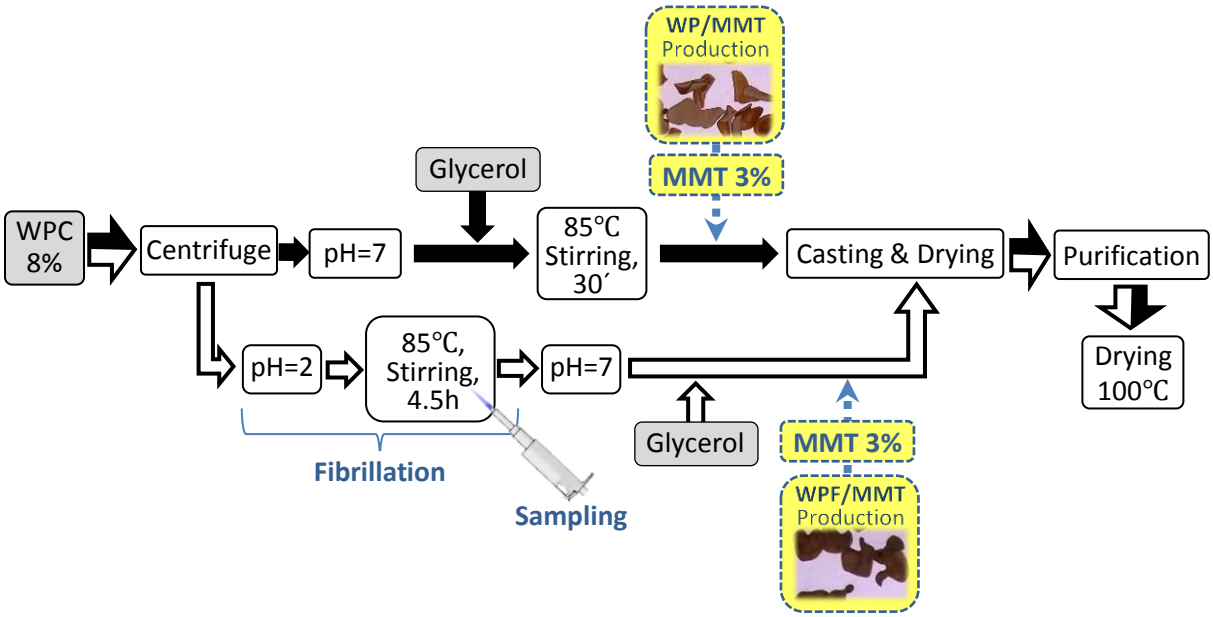

Figure 1: Main steps of WP polymer and nanocomposites production. The black-arrows show WP and WP/MMT production paths; while to produce WPF and WPF/MMT the white-arrows should be followed. To produce WP/MMT and WPF/MMT nanocomposites, dispersed MMT should be added before casting step. The black and white arrows show the common steps between the two paths.

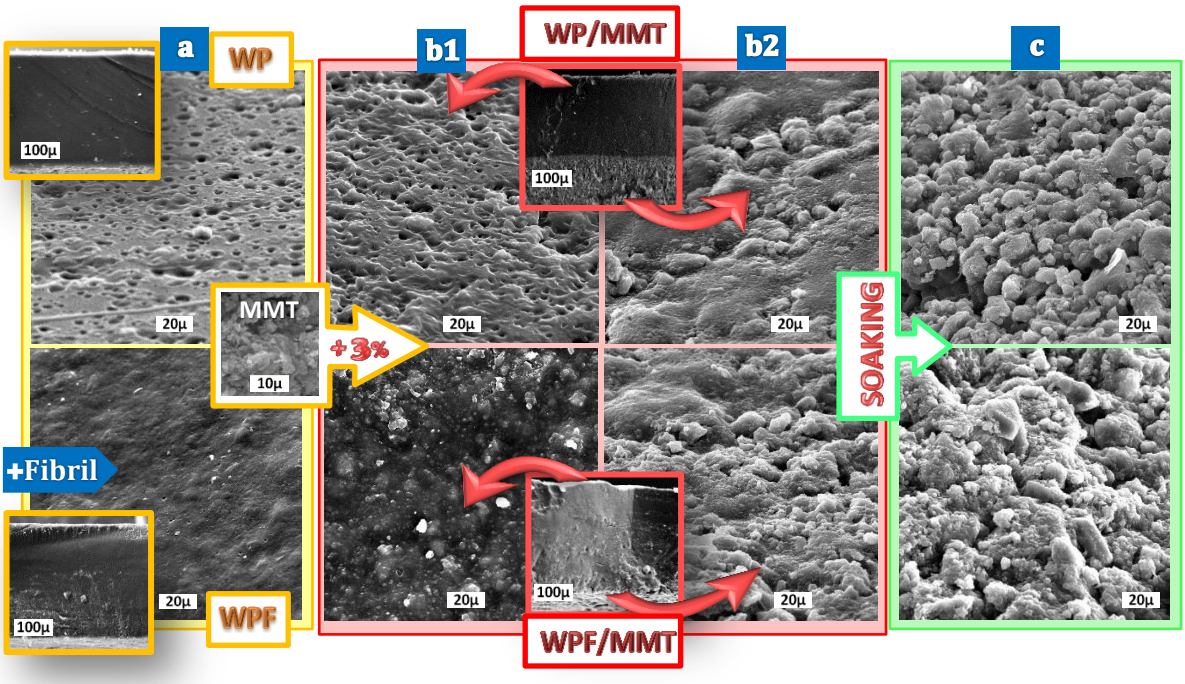

Figure 2: SEM micrographs of the surface (main images) and cross-section (smaller images) of WP polymers and composites with and without nanofibrils (top and bottom row, respectively). Column **(a)** shows WP (top) and WPF (bottom). Columns **(b1, b2)** show upward and downward sides of WP/MMT (top), and WPF/MMT (bottom), **(c)** is their upper surface after soaking in water.

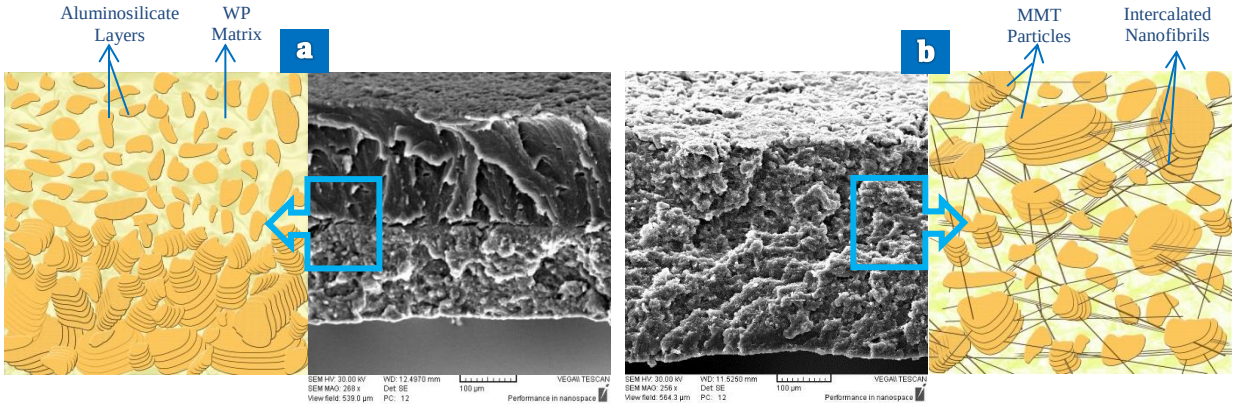

Figure 3: SEM cross-sectional micrographs (the middle images) and the sketches of our hypothesis of arrangement for **(a)** WP/MMT, and **(b)** WPF/MMT nanocomposites. The sketches suggest that in WP/MMT, MMT components settle mostly at the bottom layer. In contrast, they are well dispersed in the WP matrix in the presence of nanofibrils.

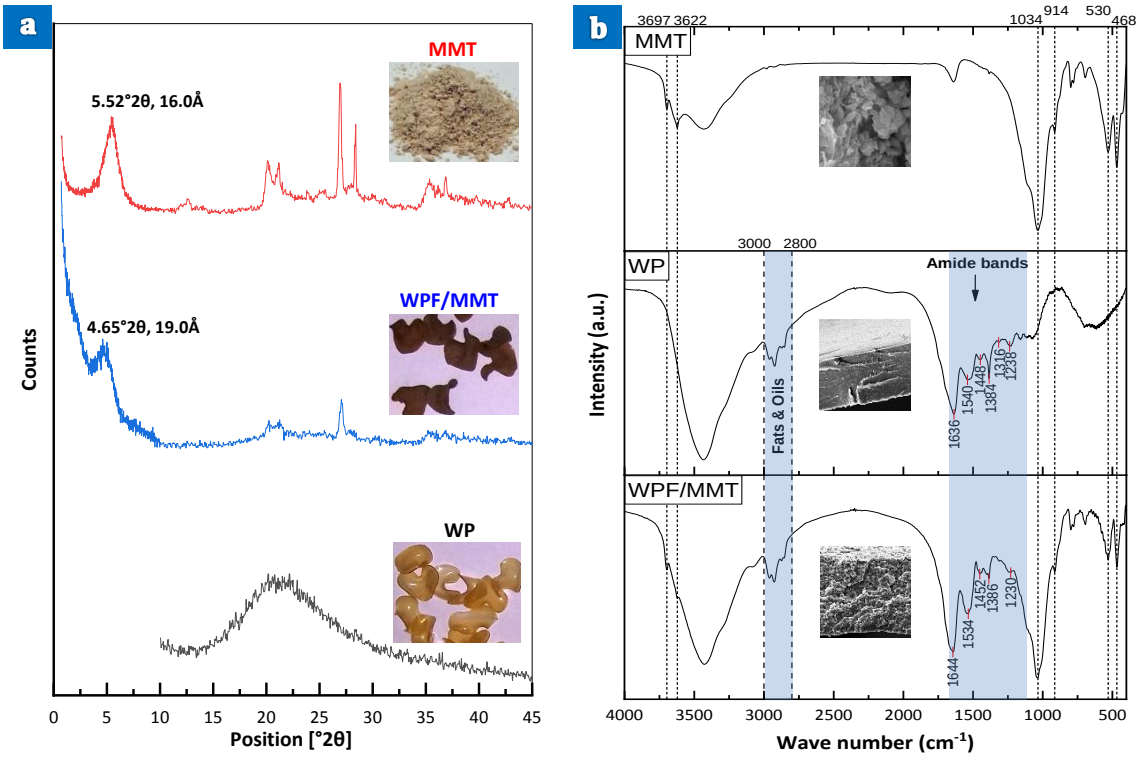

Figure 4: (a) XRD pattern of pristine MMT, WP and WPF/MMT. *Insets:* macrostructures. **(b)** FT-IR spectrum of pristine MMT, WP and WPF/MMT. Shaded areas indicate the characteristic peaks of fats and oils as well as proteins. Main peaks of MMT are found within the three pairs of stippled lines (wavenumbers are provided at the top of the graph). *Insets:* SEM structures.

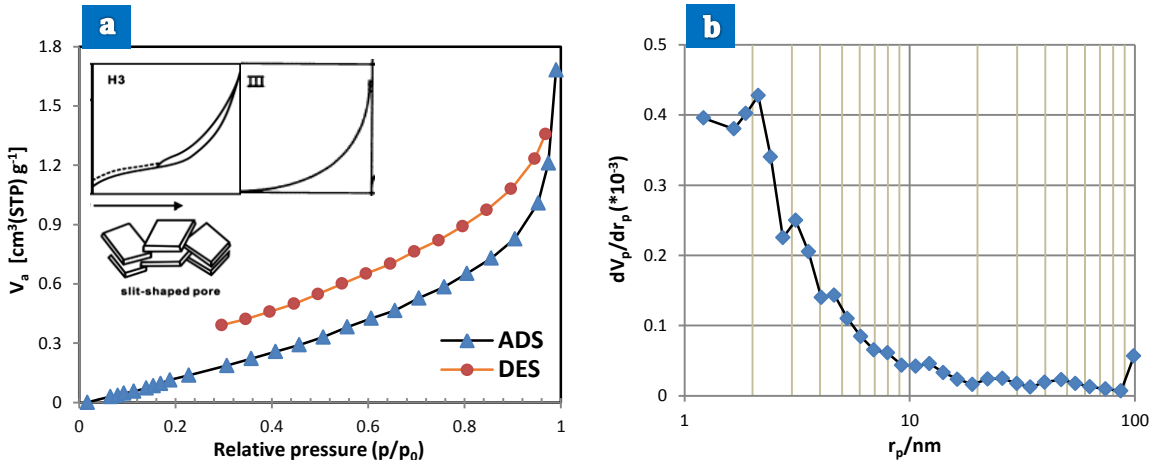

Figure 5: (a) Nitrogen adsorption/desorption isotherms (BET analysis) of the WPF/MMT Nanocomposite. Inset pictures show type III isotherm model (right) and hysteresis loop type H3 and the related pore shape (*i.e.* slit-shaped) (left) (Tang et al., 2015), and **(b)** corresponding BJH pore size distributions**.**

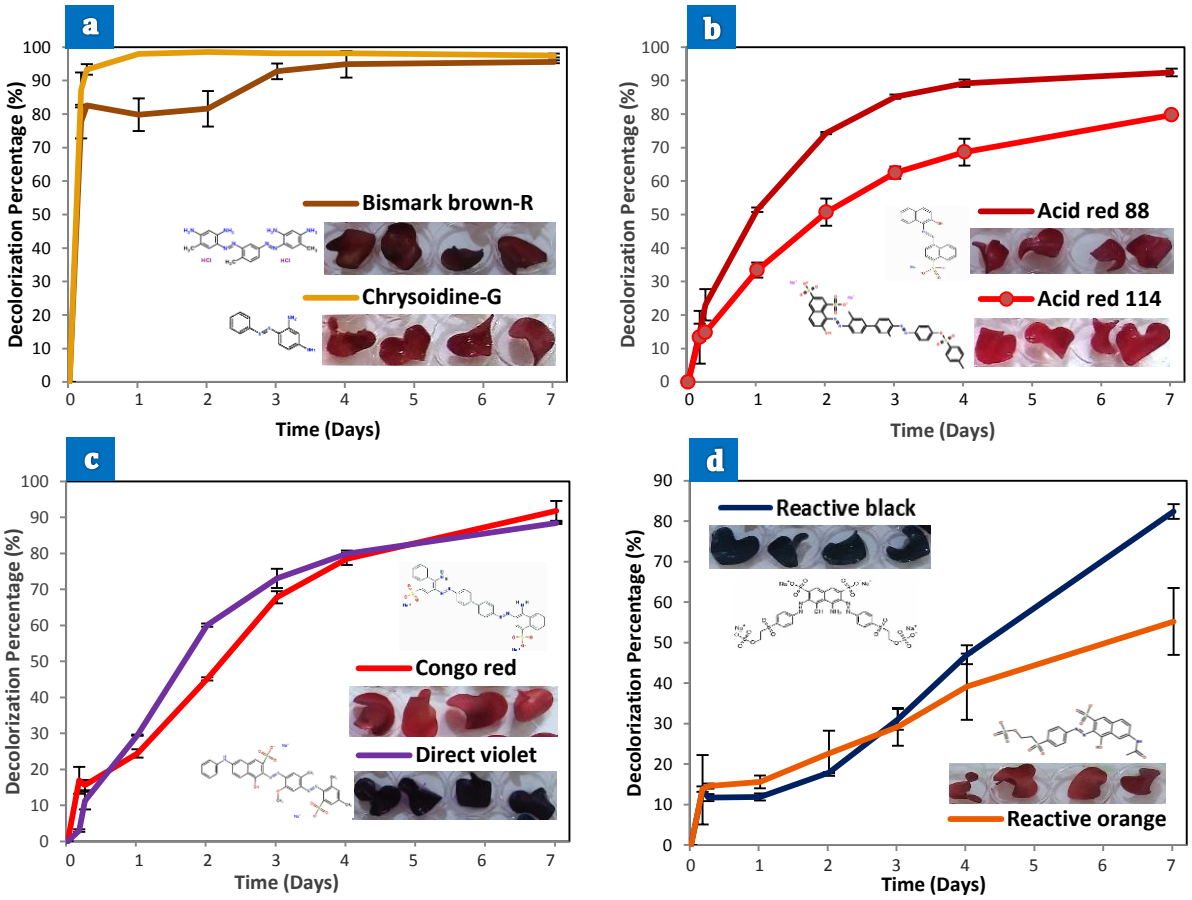

Figure 6: Adsorption of different azo dyes over time onto a 2% w/v WPF/MMT nanocomposite. **(a)** Two cationic dyes, **(b)** two acid dyes, **(c)** two direct dyes, and **(d)** two reactive dyes. In all cases, the initial dye concentration was 250 mg/L. Inset photographs show the appearance of WPF/MMT after 1 week soaked in the dye solutions. The chemical structure of the dyes is also shown.

Figure 7: Photograph of **(a)** WP, **(b)** WP/MMT and **(c)** WPF/MMT: **(1)** before, and **(2)** after soaking in water and heat treatment, **(3)** show the adsorbents after immersing in the eight azo dye solutions for a week. WP and WP/MMT swelled more than the WPF/MMT, and some of them are destroyed in some dyes' solution in a week and are absent in the figure. **(d**) The effect of heat treatment (100 °C, 1 h) *right:* WPF/MMT after heat treatment, *left:* the same material, without heat treatment; after immersing in the dyes for 4 days.

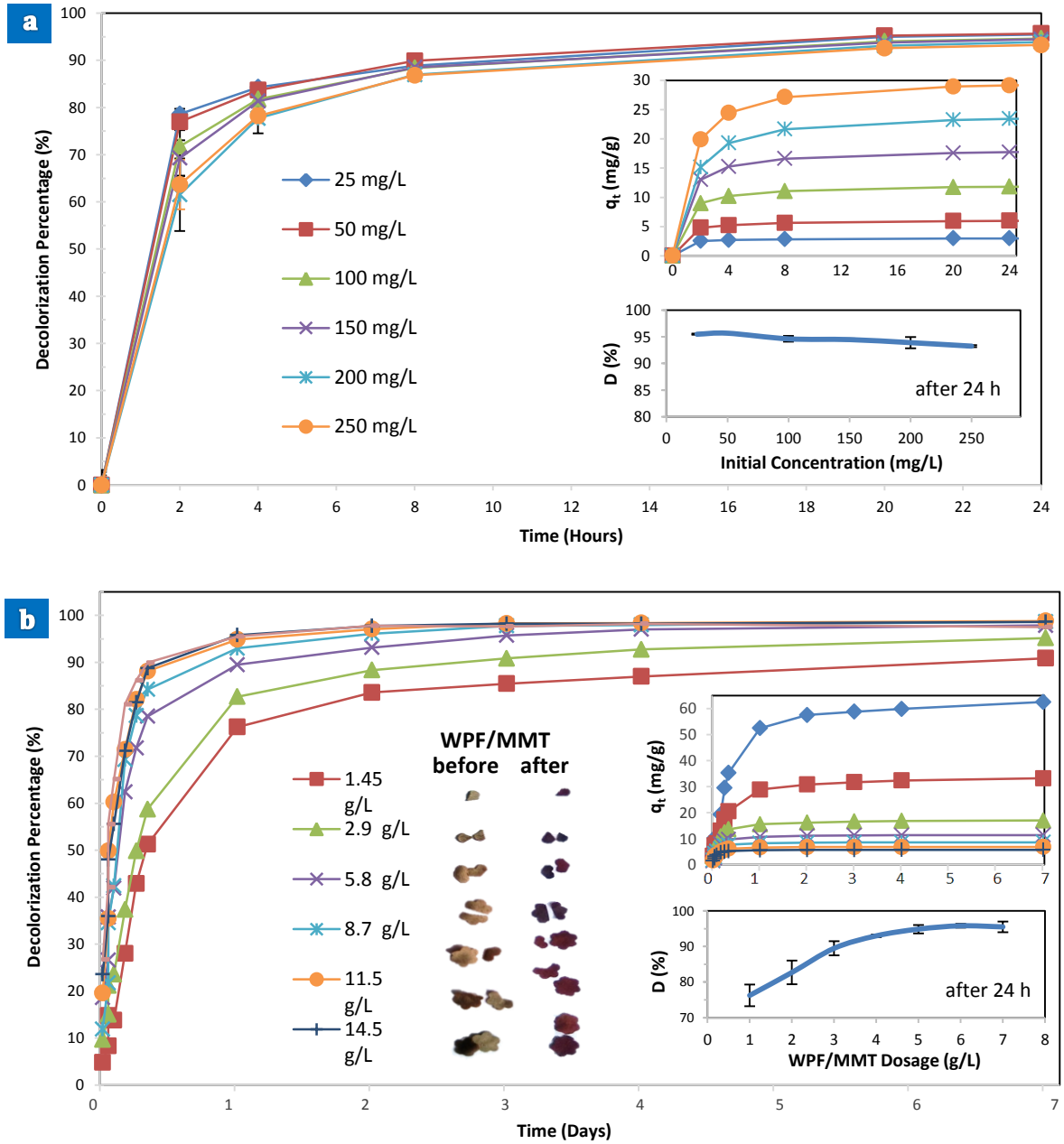

Figure 8: Effect of **(a)** dye concentration (using 8 g/L adsorbent), and **(b)** WPF/MMT dosage (using 100 mg/L dye) on Chrysoidine-G dye decolorization percentage. Amount of dye adsorbed by WPF/MMT (q_t) (upper inset graph) and the effect of WPF/MMT dosage (g/L) on adsorption percentage (lower inset graph). Inset pictures show WPF/MMT before and after the adsorption process.

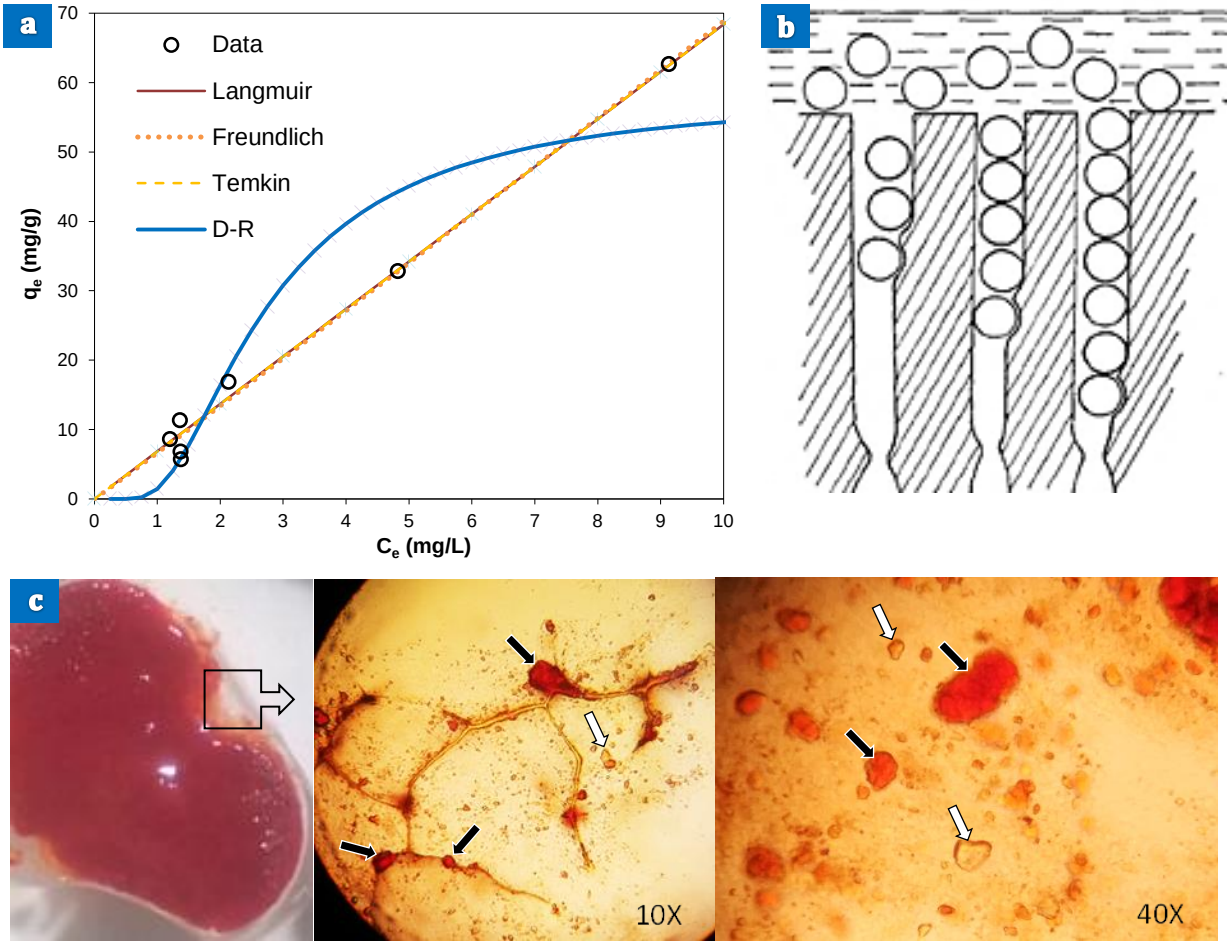

Figure 9: (a) Nonlinear adsorption isotherms of Chrysoidine-G onto WPF/MMT at 35°C. **(b)** Scheme illustrating linear isotherm (Giles, Smith, & Huitson, 1974; Giles, Smith, Huitson, & science, 1974), **(c)** microstructure of WPF/MMT after adsorption of Chrysoidine-G, Favorable places for dye aggregation: black arrows, and unfavorable places: white arrows

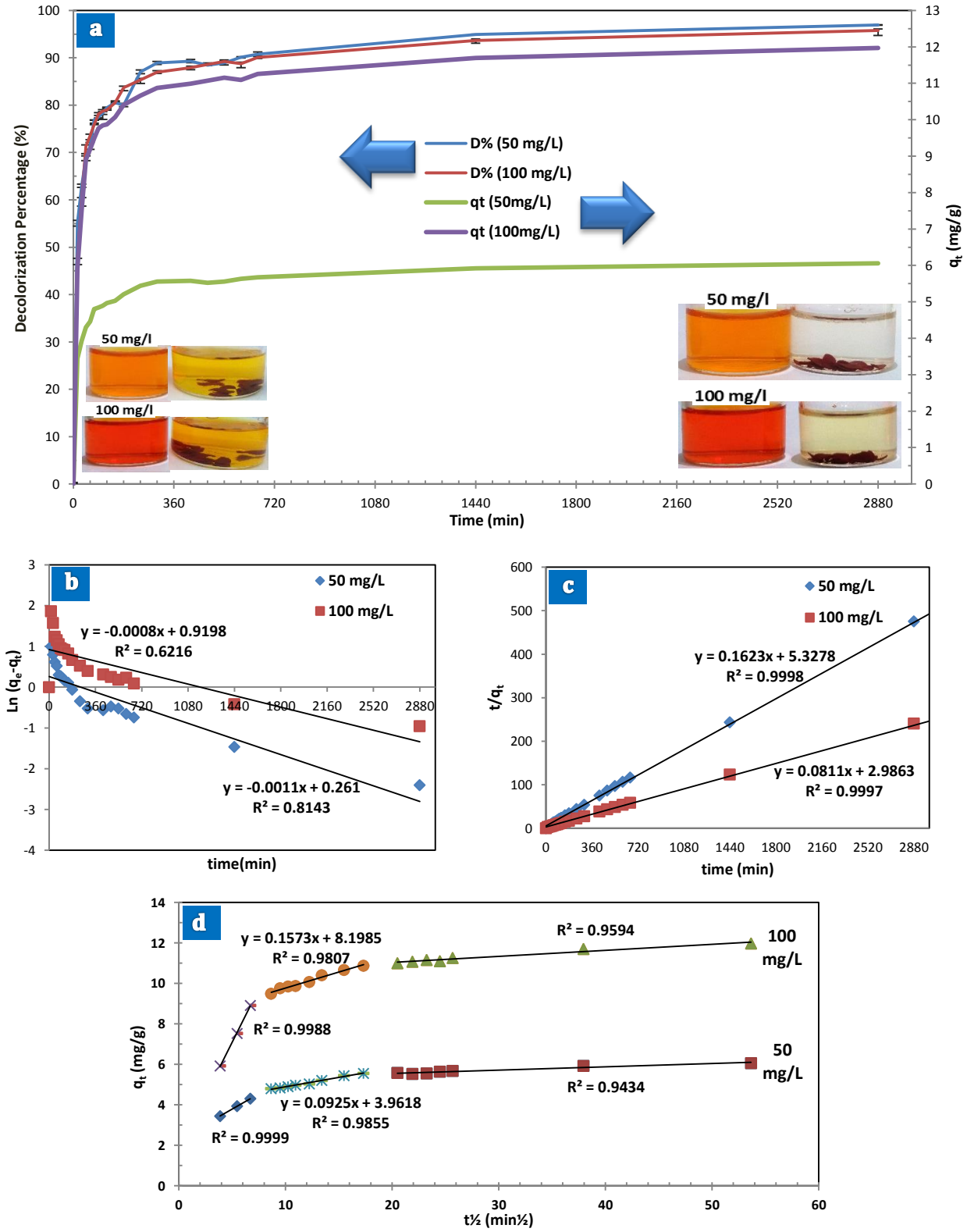

Figure 10: Kinetic study of Chrysoidine-G dye adsorption onto WPF/MMT (8 mg/L) at 35°C over 48 h, in a volume of 10mL. **(a)** Decolorization percentage and amount of dye adsorbed by WPF/MMT (q_e), inset pictures show Chrysoidine-G 50 and 100 mg/L without and with WPF/MMT after 80 minutes (left), and after 48 hours (right). **(b)** Pseudo-first-order model, **(c)** pseudo-second-order model, **(d)** intra-particle diffusion model for Chrysoidine-G adsorption onto WPF/MMT

Giles, C. H., Smith, D., & Huitson, A. (1974). A general treatment and classification of the solute adsorption isotherm. I. Theoretical. *Journal of colloid interface science, 47*(3), 755-765. doi:https://doi.org/10.1016/0021-9797(74)90252-5

Giles, C. H., Smith, D., Huitson, A. J. J. o. c., & science, i. (1974). A general treatment and classification of the solute adsorption isotherm. I. Theoretical. *47*(3), 755-765.

Tang, X., Jiang, Z., Li, Z., Gao, Z., Bai, Y., Zhao, S., & Feng, J. (2015). The effect of the variation in material composition on the heterogeneous pore structure of high-maturity shale of the Silurian Longmaxi formation in the southeastern Sichuan Basin, China. *Journal of Natural Gas Science and Engineering, 23*, 464-473. doi:10.1016/j.jngse.2015.02.031